

See discussions, stats, and author profiles for this publication at: <https://www.researchgate.net/publication/270585940>

# Doping Controls Plasmonics, Electrical Conductivity, and Carrier-Mediated Magnetic Coupling in Fe and Sn Codoped $\text{In}_2\text{O}_3$ Nanocrystals: Local Structure Is the Key

ARTICLE in CHEMISTRY OF MATERIALS · JANUARY 2015

Impact Factor: 8.35 · DOI: 10.1021/cm5040936

---

CITATION

1

---

READS

73

## 2 AUTHORS:



G Shiva Shanker

Indian Institute of Science Education and Re...

5 PUBLICATIONS 20 CITATIONS

SEE PROFILE



Bharat Tandon

Indian Institute of Science Education and Re...

3 PUBLICATIONS 10 CITATIONS

SEE PROFILE

# Doping Controls Plasmonics, Electrical Conductivity, and Carrier-Mediated Magnetic Coupling in Fe and Sn Codoped $\text{In}_2\text{O}_3$ Nanocrystals: Local Structure Is the Key

G. Shiva Shanker,<sup>†,‡</sup> Bharat Tandon,<sup>†,‡</sup> Tomohiro Shibata,<sup>§,¶</sup> Soma Chattopadhyay,<sup>§,¶</sup> and Angshuman Nag<sup>\*,†</sup>

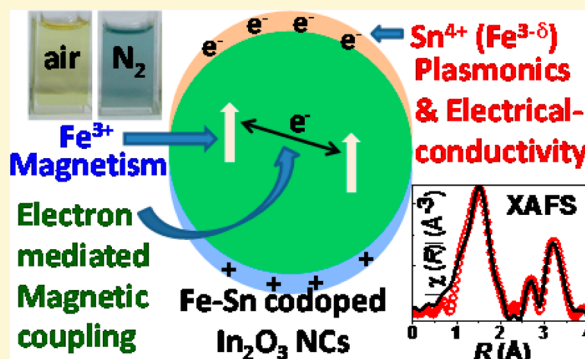
<sup>†</sup>Department of Chemistry, Indian Institute of Science Education and Research (IISER), Pune, Maharashtra 411008, India

<sup>§</sup>MRCAT, Sector 10, Bldg 433B, Argonne, National Laboratory, Argonne, Illinois 60439, United States

<sup>¶</sup>CSRRI & Department of Physics, Advanced Materials Group, Illinois Institute of Technology, Chicago, Illinois 60616, United States

**S** Supporting Information

**ABSTRACT:** Multifunctional Fe–Sn codoped  $\text{In}_2\text{O}_3$  colloidal nanocrystals simultaneously exhibiting localized surface plasmon resonance band, high electrical conductivity, and charge mediated magnetic coupling have been developed. Interactions between Sn and Fe dopant ions have been found critical to control all these properties. Sn doping slowly releases free electrons in the colloidal nanocrystals, after reduction of active complex between  $\text{Sn}^{4+}$  and interstitial  $\text{O}^{2-}$ . Unexpectedly, Fe codoping reduces the free electron concentration. Our X-ray absorption fine structure spectroscopy (XAFS) results show that  $\text{Fe}^{3+}$  and  $\text{Sn}^{4+}$  substitutes  $\text{In}^{3+}$  in the  $\text{In}_2\text{O}_3$  lattice for all Fe-doped  $\text{In}_2\text{O}_3$  NCs and Sn-doped  $\text{In}_2\text{O}_3$  NCs. Interestingly, for Fe–Sn codoped NCs, a smaller fraction of  $\text{Fe}^{3+}$  gets reduced to  $\text{Fe}^{2+}$  by consuming free electrons produced by Sn doping. Therefore, Fe doping can manipulate free electron concentration in Fe–Sn codoped  $\text{In}_2\text{O}_3$  nanocrystals, controlling both plasmonic band and electrical conductivity. Free electrons, on the other hand, facilitate magnetic coupling between distant  $\text{Fe}^{3+}$  ions. Such charge mediated magnetic coupling is useful for spin-based applications.



## INTRODUCTION

There is only one recent report of Fe–Sn codoped  $\text{In}_2\text{O}_3$  nanocrystals (NCs) exhibiting the combination of localized surface plasmon resonance (LSPR) in near to mid infrared region and weak ferromagnetism at room temperature.<sup>1</sup> Sn doping provides free electrons for LSPR and Fe doping provides magnetic spin. In this paper, we control the interaction between two kinds of dopants in Fe–Sn codoped  $\text{In}_2\text{O}_3$  nanocrystals, via probing the atomic bonding and ion valence of dopant ions. Such interactions essentially control properties like LSPR, free carrier mediated magnetism, and electrical conductivity. To the best of our knowledge, our Fe and Sn codoped  $\text{In}_2\text{O}_3$  NCs are the only system reported so far, that can simultaneously exhibit tunable LSPR, high electrical conductivity ( $>1$  S/cm), and charge controlled magnetic coupling at room temperature, along with solution processability and optical transparency in visible range.

The coexistence of near-infrared (NIR) LSPR and room temperature ferromagnetism was achieved by making heterostructured NCs such as  $\text{Fe}_3\text{O}_4/\text{Au}$  or  $\text{Fe}_3\text{O}_4/\text{Cu}_{2-x}\text{S}$  core/shell NCs; however, significant interaction has not been observed between the free electrons exhibiting LSPR and magnetic spins.<sup>2–5</sup> A doped system, like Fe–Sn codoped  $\text{In}_2\text{O}_3$  NCs, with homogeneity in composition throughout the NC can offer

a better possibility of such interactions. Manipulation of 50 interactions between the free electrons and magnetic spin can 51 lead to spin-based information processing devices from 52 solution-processed NCs.<sup>6</sup> Also, there is a possibility to derive 53 fundamentally new magneto-optic properties via interactions of 54 plasmonic and magnetic responses. 55

In Fe–Sn codoped  $\text{In}_2\text{O}_3$  NCs,  $\text{Sn}^{4+}$  provides free electron in 56 the conduction band of  $\text{In}_2\text{O}_3$  NCs, which in turn leads to 57 LSPR and electrical conductivity.<sup>7–11</sup>  $\text{Fe}^{3+}$  doping on the other 58 hand leads to magnetic properties owing to five unpaired 59 electrons in high spin states.<sup>12</sup>  $\text{Fe}^{3+}$  doping alone is not known 60 to influence LSPR; however, when codoped with Sn in  $\text{In}_2\text{O}_3$  61 NCs, both LSPR and electrical conductivity of our NCs change 62 systematically with Fe concentration. Such an observation is 63 not intuitive. On the other hand, Sn doping influences the 64 magnetic properties of Fe–Sn codoped  $\text{In}_2\text{O}_3$  NCs, which is 65 again not obvious. The scenario becomes even more 66 complicated for nanocrystal samples, because the dopant ions 67 can reside in different environments, namely, in lattice 68 substituted bulk, or bound to the NC surface, or even in the 69

Received: November 6, 2014

Revised: January 3, 2015

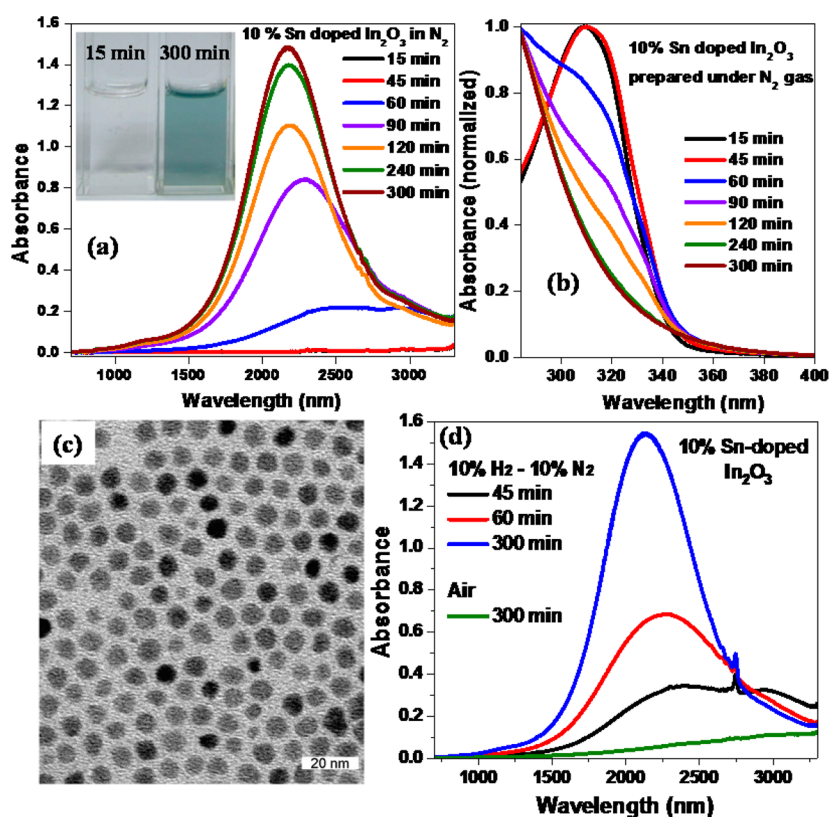


**Figure 1.** Variation of (a) the LSPR band and (b) excitonic transition with time of reaction for colloidal 10% Sn-doped  $\text{In}_2\text{O}_3$  NCs carried under  $\text{N}_2$  atmosphere. (c) TEM image of 10% Sn-doped  $\text{In}_2\text{O}_3$  NCs carried under  $\text{N}_2$  atmosphere isolated after 60 min. (d) Comparison of LSPR data of 10% Sn-doped  $\text{In}_2\text{O}_3$  NCs prepared under air (oxidizing conditions) and under mixture of 10%  $\text{H}_2$ –90%  $\text{N}_2$  gas (reducing atmosphere).

interstitial sites.<sup>13</sup> Clearly, a microscopic elucidation of atomic bonding and ion valence is the key to understand the origin of various properties and, thereby, controlling the properties for a desired application. Size of our NCs (6.5 nm) is too small to measure single-crystal X-ray diffraction (XRD). Furthermore, powder XRD peak also broadens up for NCs; therefore, quantitative estimation of lattice doping using Vegard's law becomes difficult. We employed synchrotron based extended X-ray absorption fine structure (EXAFS) and X-ray absorption near edge structure (XANES) spectroscopy to study such local coordination and ionic charge.<sup>14–17</sup> Importantly, EXAFS can also probe any noncrystalline impurity that may be present in the sample, which cannot be probed by XRD.

Our results show that Sn and Fe are lattice substituted for all doped NC samples. The slow reduction of active complex of  $\text{Sn}^{4+}$ -interstitial oxygen generates free electrons in the conduction band of  $\text{In}_2\text{O}_3$  host NC. Fe remains in 3+ oxidation state for all Fe-doped  $\text{In}_2\text{O}_3$  NCs; however, for Sn–Fe codoped samples, a smaller fraction of  $\text{Fe}^{3+}$  gets reduced to  $\text{Fe}^{2+}$  by consuming free electrons. Consequently, Fe doping can manipulate free carrier concentration, thereby, influencing both LSPR and electrical conductivity. Electron paramagnetic resonance (EPR) data show the existence of charge mediated magnetic coupling in Fe–Sn codoped NCs, where free electrons arising from  $\text{Sn}^{4+}$  can mediate magnetic coupling between distant Fe ions.

## EXPERIMENTAL SECTION

Colloidal Sn and Fe codoped  $\text{In}_2\text{O}_3$  NCs were synthesized following our previous report.<sup>1</sup> Stoichiometric amounts of In, Fe, and Sn precursors were taken to get desired composition of NCs. For

example, in order to prepare 10% Sn–10% Fe codoped  $\text{In}_2\text{O}_3$  NCs, 0.24 mmol of indium(III) acetylacetonate, 0.03 mmol of iron(III) acetylacetonate, and 0.03 mmol of tin(IV) bis(acetylacetonate) dichloride were mixed with 10 mL of oleylamine in a 50 mL three-necked round-bottom flask. First the reaction mixture was subjected to  $\text{N}_2$  atmosphere and vacuum alternatively for 30 min at room temperature followed by degassing at high vacuum for 30 min at 100 °C. The temperature of the reaction mixture was gradually increased to 220 °C under  $\text{N}_2$  gas atmosphere and kept undisturbed for 5 h. The solution was cooled to room temperature, and then an adequate amount (~30 mL) of methanol was added as a nonsolvent to precipitate NCs followed by centrifugation at 5000 rpm for 5 min. The obtained NCs were redispersed in toluene and were precipitated again using methanol; the washing process was repeated twice. A detailed elemental analysis showed that precursor concentrations of dopant is the same as dopant concentrations in the final NC within experimental errors;<sup>1</sup> therefore, the precursor concentration has been mentioned through the manuscript for all NCs. The high level of doping obtained in our NCs might result from prebonded In–O, Fe–O, and Sn–O moieties in precursors.<sup>18,19</sup> We have also carried out reactions in an environment other than  $\text{N}_2$  gas, such as in air, and a mixture of gases with 10%  $\text{H}_2$  and 90%  $\text{N}_2$ .

UV–visible–NIR absorption spectra of NCs dispersed in tetrachloroethylene was measured using both PerkinElmer Lambda-950 UV/vis spectrometer and Lambda-45 UV/vis spectrometer. Powder XRD patterns were recorded by employing a Bruker D8 Advanced X-ray diffractometer using  $\text{Cu K}\alpha$  radiation (1.54 Å). Transmission Electron Microscopy (TEM) images were obtained using a JEOL JEM 2100F microscope operated at 200 kV. Energy Dispersive X-ray Analysis (EDAX) of the NCs were done using Zeiss Ultra Plus scanning electron microscopy Instrument. X-band EPR spectra was determined on a Bruker-ER073 spectrometer equipped with an EMX microX source. Four probe dc electrical conductivity measurements were performed on NC pellets using a Keithley Four-Probe

Conductivity Instrument (Model 6220/6221 Current Source and Model 2182A nanovoltmeter). Here we made point contacts between the tip of the probe and the surface of circular pellets. The probes were collinear, equally spaced (2.0 mm), and each having a diameter of 0.54 mm. These pellets were annealed at 200 °C inside the glovebox for 1 h removing residual solvents but without changing the crystallite size. The conductivity,  $\sigma = 1/\rho$ , where  $\rho$  is resistivity and is given by the equation  $\rho = 2\pi s(V/I)/f(w/s)$ , where  $V$ ,  $I$ , and  $s$  are voltage, current, and spacing between electrodes, respectively, and  $f(w/s)$  is a function of width of the pellet ( $w$ ) and  $s$ .<sup>20</sup> The uncertainty in  $f(w/s)$  might result in some error in the calculated value of conductivity; however, any such possible inaccuracy does not influence the present study. XANES and EXAFS data were measured at 10ID undulator beamline at Advanced Photon Source in Argonne National Laboratory.<sup>21</sup> The typical beam size was 500  $\mu\text{m} \times 500 \mu\text{m}$ . Fe K edge data were measured in fluorescence mode using an ion chamber with Stern Heald geometry.<sup>22</sup> The energy calibration was done with Fe foil at the first inflection point of 7111 eV, and data for samples were aligned with reference Fe foil placed between transmission and reference ion chamber. Rhodium coated harmonic rejection mirror was used for eliminating higher energy X-rays. Well-known self-absorption error was ensured negligible with the comparison with the transmission data because of heavy elements (In and Sn) in the samples. Standard  $\text{Fe}_2\text{O}_3$  and FeO were measured with transmission geometry. For In K edge (27940 eV) and Sn K edge (29200 eV) measurements were also performed with transmission geometry. Pt coated harmonic rejection mirror was used. For Fe, In, and Sn K edge measurements, incident monitor ion chamber was filled with gas optimized for 5% absorption and transmission ion chamber was 20% absorption at respective energies, ensuring the linearity of the detector sets. The EXAFS signals  $\chi(k)$ , with  $k$  being a photoelectron wavenumber, were extracted in a conventional way using the ATHENA program.<sup>23</sup>  $k^2$  weight  $\chi(k)$  were Fourier transformed to real space  $\chi(R)$ , and coordination numbers, bond lengths, and bond lengths distribution (Debye–Waller factor) parameters were obtained by fitting to a model constructed using ab initio calculation code FEFF6 using the ARTEMIS program.<sup>23</sup> The EXAFS spectra were fit in real space  $\chi(R)$  including two coordination shells.

## RESULTS AND DISCUSSION

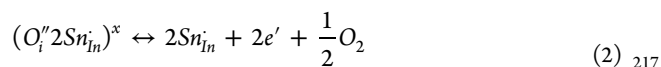
**Slow Generation of Free Electrons in Colloidal Sn-Doped  $\text{In}_2\text{O}_3$  NCs.** Figure 1a and 1b show the UV–visible–NIR absorption data of Sn-doped  $\text{In}_2\text{O}_3$  NCs prepared under  $\text{N}_2$  atmosphere at different reaction times. The absorption edge in the UV region (Figure 1b) corresponds to the optical gap of the semiconductor, and the NIR absorption (Figure 1a) is due to the LSPR band of free electrons. Clearly, the LSPR band is absent for reaction time up to 45 min. The LSPR band appears at 60 min and then shifts toward a shorter wavelength along with an increasing absorbance as the reaction proceeds. Correspondingly, the tail of the LSPR band absorbs red-light, imparting the complementary blue color to the reaction mixture after 60 min, and the color became more intense with increasing reaction time (inset of Figure 1). According to the Drude model, the LSPR band is expected to shift toward shorter wavelength and become more intense (higher absorbance) with an increase in free electron density.<sup>24</sup> Therefore, it can be concluded that the free electrons start appearing slowly during the course of reaction. The influence of this slow release of free electrons is also observed in the optical gap of NCs in the UV region (Figure 1b). As the reaction time increases, the sharp excitonic feature bleaches because the generated free electrons screen the Coulomb attraction between electron–hole pair.<sup>25,26</sup> Also, the generation of free electrons in the conduction band typically widens the optical gap of Sn-doped  $\text{In}_2\text{O}_3$  NCs because of the Burstein–Moss

effect,<sup>7,24</sup> and such a widening of the optical gap is also observed (Figure 1b) with a longer reaction time after 60 min. What is the mechanism of this slow generation of free electrons in our NCs? In order to address this question, let us first discuss the mechanism of free electron generation in bulk Sn-doped  $\text{In}_2\text{O}_3$ . One oxygen vacancy can give rise to two electrons following eq 1<sup>27</sup>



where  $\text{O}_\text{O}^\times$  represents a neutral oxygen on an oxygen site;  $V_\text{O}$  represents a vacancy with charge of +2 on an oxygen site, and  $e'$  represents an electron with charge  $-1$ . However, the amount of oxygen vacancies is typically low ( $<0.5\%$ ). So far, colloidal synthesis of  $\text{In}_2\text{O}_3$  NCs has not lead to the formation of enough free electrons from oxygen vacancies, and therefore the LSPR band has not been observed for  $\text{In}_2\text{O}_3$  NCs.

On the other hand, each  $\text{Sn}^{4+}$  provides one free electron in the conduction band of bulk Sn-doped  $\text{In}_2\text{O}_3$  with the doping level up to 5–10% following eq 2<sup>28</sup>



where  $\text{Sn}_\text{In}$  represents a positively charged Sn on an In site (basically substitution of  $\text{In}^{3+}$  with  $\text{Sn}^{4+}$  leads to 1+ charge in the crystal), and  $\text{O}_\text{i}'$  represents an interstitial oxygen with  $-2$  charge. Typically, one interstitial oxygen is accompanied by two  $\text{Sn}^{4+}$  ions substituting two  $\text{In}^{3+}$  ions, maintaining the charge neutrality, which subsequently can get reduced following eq 2. At higher levels of Sn doping, the neutral  $(\text{O}_\text{i}'2\text{Sn}_\text{In})^\times$  centers can undergo clustering forming a more stable product which does not get reduced following eq 2 and, therefore, decreases the effective free electron concentration.<sup>29</sup>

In our NCs, the slow generation of free electron can be because of multiple reasons such as (i) slow rate of formation of nanocrystals or (ii) even though the host NC is formed instantaneously, the rate of Sn doping can be slower, or (iii) slower reduction of active Sn dopant following eq 2. Figure S1 of the Supporting Information (SI) shows similar XRD patterns for all NCs throughout the synthesis starting from 15 to 300 min, which matches with the cubic bixbyite structure of  $\text{In}_2\text{O}_3$  (JCPDS no. 88-2160, space group  $Ia3$ ). The TEM image in Figure 1c shows the average diameter NCs size is 6.5 nm after 60 min of reaction, and the size remains similar even after 300 min (Figure S2a in the SI). So, growth of host NCs is already over by 60 min of reaction, and the release of free electrons after 60 min is not due to slow NC growth. EDAX data exhibit a similar Sn content of 8.1 and 9.4% for samples obtained after 60 and 300 min of reactions. Similarly, ICP-OES (inductively coupled plasma–optical emission spectroscopy) 9.3 and 10.1% Sn for samples obtained after 60 and 300 min of reactions. It is to be noted that such elemental analysis cannot distinguish between dopant ions on the surface of NCs and lattice substituted dopants at the core of NCs. However, Milliron et al.<sup>11</sup> recently demonstrated that the surface bound Sn dopants exhibit narrower LSPR spectrum compared to Sn doped in the core of the  $\text{In}_2\text{O}_3$  NC lattice. Figure 1a does not show any broadening of the LSPR peak with increasing reaction time, therefore suggesting that the diffusion of dopant ions from surface toward the core of NCs is not a plausible reason for the emergence of the LSPR band with reaction time. Therefore, slower or inhomogeneous Sn incorporation is also not the cause of slow release of free electrons.



To verify the third possibility, i.e., slow reduction of active Sn dopant following eq 2, we carried out the colloidal synthesis with different oxygen partial pressure: in air, under  $N_2$  gas, and under reducing (90%  $N_2$  and 10%  $H_2$ ) gas. Such a change in the reaction environment neither changes the NC size (TEM images in Figure S2 of SI) nor the extent of Sn doping ( $\sim 10\%$ ) obtained from EDAX and ICP-OES. Figure 1d shows that the LSPR band is almost absent for Sn-doped  $In_2O_3$  NCs when the reaction is carried out in air. Consequently, the color of the NC prepared in air is also not blue (inset to Figure S2b in the SI). On the other hand, with reducing conditions (90%  $N_2$  and 10%  $H_2$ ), the LSPR band appears in about 45 min (Figure 1d) of reaction time, which is quicker compared to 60 min required to observe LSPR for reactions carried out under  $N_2$  (Figure 1a). Evidently, a lower partial pressure of oxygen during the synthesis favors the reduction of active Sn dopant following eq 2. The slow release of free carriers during colloidal synthesis is because of the slow reduction process shown in eq 2. It is to be noted that such reduction in bulk Sn-doped  $In_2O_3$  also takes many hours at an elevated temperature.<sup>28</sup>

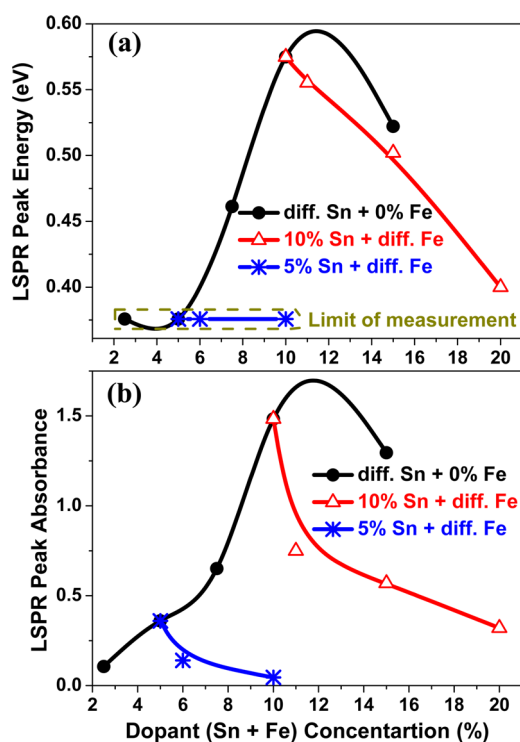
### Effect of Fe Codoping on Free Carrier Concentration.

Figure 2 (and Figure S3 in the SI) shows how the LSPR peak energy and peak absorbance can be controlled by controlling the doping concentrations of Sn and Fe codoped  $In_2O_3$  NCs. Both  $In_2O_3$  and Fe-doped  $In_2O_3$  NCs do not exhibit any LSPR and are not mentioned in Figure 2. For samples with 0% Fe and

different concentrations of Sn (black solid circle), both LSPR peak energy and absorbance increase systematically with increasing Sn content up to 10%, qualitatively following the Drude model. However, both LSPR peak energy and absorbance decrease with a further increase in Sn concentration beyond 10%. This is a commonly observed phenomenon and is attributed to trapping of free electrons around  $Sn^{4+}$  because of clustering of  $(O_i^{2-}2Sn_{In}^{4+})^x$  centers at a high level of doping, as discussed in the previous subsection.<sup>8,24</sup> For samples with 10% Sn and different amounts of Fe (red, open triangle), both LSPR peak energy and absorbance decreases with increasing Fe content, a phenomenon also observed in our prior report, ref 1. At a lower level of total doping ( $\leq 10\%$ ), for example, samples with 5% Sn and different Fe content, the LSPR absorbance decreases sharply with increasing Fe content (Figure 2b). Clearly, for all doping concentrations of Fe–Sn codoped NCs, an increase in Fe content systematically decreases both LSPR absorbance and peak energy. Therefore, the mechanism by which Fe doping influences the LSPR band is probably different from the electron trapping mechanism around Sn centers observed only with higher levels ( $>10\%$ ) of doping in Sn-doped  $In_2O_3$  NCs.

The size and shape of Sn doped and Sn–Fe codoped NCs are similar.<sup>1</sup> Capping ligands and solvent are the same for all samples. Furthermore, all samples were dilute having similar concentration, and, therefore, any influence of inter-NC distance on the LSPR is not expected. Also, dielectric constant of NCs is not expected to change much by a small amount of Fe doping, for example, 1% Fe codoped with 10% Sn shows significant influence on the LSPR band, which cannot be explained by the change of dielectric constant. Therefore, none of the above factors can explain the observed changes in LSPR. Therefore, a probable decrease in free electron concentration with increasing Fe dopant concentration can explain the observed LSPR properties.

Apart from LSPR, free electrons also control the electrical conductivity. Figure 3 shows four-probe electrical conductivity measurements on  $\sim 1$  mm thick pellets of Fe and Sn codoped  $In_2O_3$  NCs. Linear voltage ( $V$ ) vs current ( $I$ ) plots are observed for all the samples. Interestingly, slope of the plots, which signify resistance following the Ohm's law, increases with increasing Fe content. The calculated conductivity values obtained from these samples decreases systematically from 35



**Figure 2.** Plots of LSPR (a) peak energy and (b) peak absorbance for Sn–Fe codoped NCs with different concentrations. Black circles show the effect of Sn doping without having any Fe. Red open triangles show the effect of Fe doping in NCs having a constant 10% Sn, and blue stars show the effect of Fe doping in NCs having a constant 5% Sn. Colored lines are just guides for eyes. Codoped samples with 5% Sn and a varying amount of Fe do not show a clear LSPR peak within our measurement limit of  $<3300$  nm (0.376 eV), and the LSPR absorbance at 3300 nm has been plotted (blue stars) in part b, for such samples.

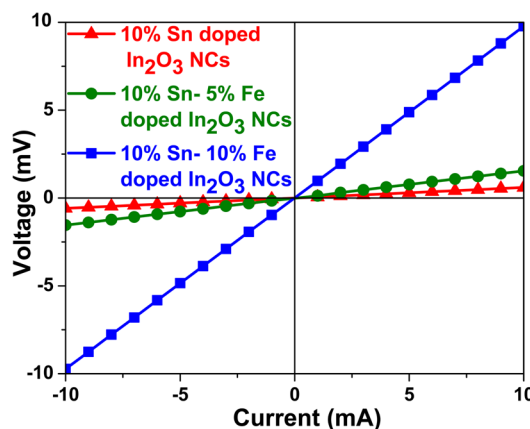


**Figure 3.** Voltage vs current plots for doped NC samples after making pellets. Symbols are experimental data, and lines are just a guide to the eye.

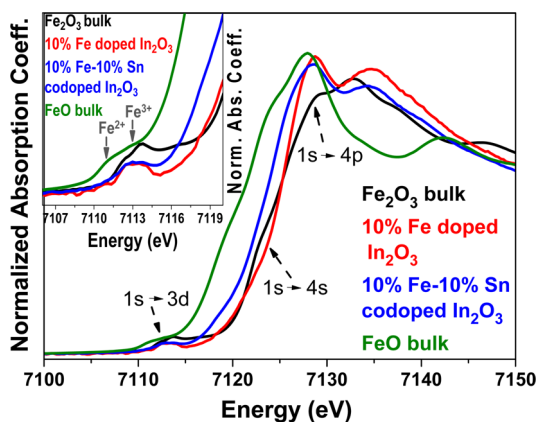


**Figure 4.** Fe K edge XANES data for different Fe–Sn codoped  $\text{In}_2\text{O}_3$  NCs. Data from NCs were compared with known reference samples. Bulk  $\text{Fe}_2\text{O}_3$  and bulk  $\text{FeO}$  exhibit +3 and +2 oxidation states for Fe. Inset compares the pre-edge data for different samples after magnifying a narrow spectral region shown in the mainframe.

coordination environment around  $\text{Fe}^{3+}$  ions in NCs owing to lattice doping.

The crest of the edge shifted toward lower energy when Sn is codoped with Fe, as shown in Figure 4. For 10% Sn–10% Fe codoped  $\text{In}_2\text{O}_3$  NCs with equal amounts of Sn and Fe, the shift of the main crest is small (about 0.3 eV) compared to 10% Fe doped  $\text{In}_2\text{O}_3$  NCs, but the edge of the codoped sample broadens with more contribution from lower energy side. Such lower energy contribution suggests reduction of some of the  $\text{Fe}^{3+}$  ions to  $\text{Fe}^{2+}$  (or  $\text{Fe}^{3-\delta}$ ) in the presence of Sn in the codoped sample.<sup>36</sup> A similar partial reduction of  $\text{Fe}^{3+}$  to  $\text{Fe}^{2+}$  was also observed in Fe–Cu codoped bulk  $\text{In}_2\text{O}_3$  NCs when prepared under a low  $\text{O}_2$  partial pressure. We note here that the increase in lattice disorder can also broaden the XANES spectrum;<sup>37</sup> however, signatures of such lattice disorder (broadening) are not observed in Sn (Figure S5 in the SI) and In edges (not shown) obtained from the same Fe–Sn codoped NCs. Compared to  $\text{FeO}$ , XANES of 10% Sn–10% Fe codoped  $\text{In}_2\text{O}_3$  NCs is at a significantly higher energy suggesting the majority of Fe in the codoped sample is still in the  $\text{Fe}^{3+}$  state, while a smaller fraction has got reduced to  $\text{Fe}^{2+}$  (or  $\text{Fe}^{3-\delta}$ ). The pre-edge position (inset to Figure 4a) of the codoped sample also remains at 7113 eV suggesting the dominance of  $\text{Fe}^{3+}$  ions in the codoped NCs.<sup>36</sup> XANES data (not shown) for the 5% Fe–10% Sn codoped sample also suggest a similar partial reduction of  $\text{Fe}^{3+}$  ions. The partial reduction of  $\text{Fe}^{3+}$  even in the presence of excess Sn suggests that a fraction of  $\text{Fe}^{3+}$  is somehow easily reducible. The exact origin of this preferential reduction of a fraction of  $\text{Fe}^{3+}$  is not understood presently, but probably surface Fe ions are behaving differently compared to Fe ions in the core. We note here that the observed change in Fe XANES with Sn codoping again suggests that both Fe and Sn are part of the same crystal, i.e., codoped in  $\text{In}_2\text{O}_3$  NCs, rather than causing unwanted phase segregation.

Visual inspection of the representative Fe-edge EXAFS data in Figure 5 shows that the spectrum for Fe doped and Fe–Sn codoped NCs are similar and very different from both  $\alpha\text{-Fe}_2\text{O}_3$  and  $\text{FeO}$  reference samples. Here  $k^2\chi(k)$  and their Fourier transform between  $k = 2\text{--}13 \text{ \AA}^{-1}$  to real space data  $|\chi(R)|$  are shown in panels (a), and (b), respectively, along with the best fit results. The fit was done for  $\chi(R)$  between  $R = 1\text{--}4 \text{ \AA}$ ,

S/cm for 10% Sn doped  $\text{In}_2\text{O}_3$  NCs to 14 S/cm and 2 S/cm for 10% Sn–5% Fe and 10% Sn–10% Fe codoped NCs, respectively. A similar decrease in electrical conductivity was also observed (not shown) for 5% Sn–5% Fe codoped  $\text{In}_2\text{O}_3$  NCs compared to 5% Sn doped  $\text{In}_2\text{O}_3$  NCs. The decrease in electrical conductivity with Fe doping for all doping concentrations can again be explained by a probable decrease in free electron concentration with Fe-doping; however, scattering of electrons by Fe dopants can also influence the electrical conductivity. Concentration of free electron was calculated from the corresponding LSPR band following ref 30, and the carrier mobility can be calculated using the equation  $\mu_e = 1/\rho e N_{\text{opt}}$  where  $\mu_e$  refers to electron mobility,  $\rho$  represents the resistivity of the sample,  $e$  is the electronic charge, and  $N_{\text{opt}}$  is carrier concentration. Table S1 in the SI shows both the carrier concentration and carrier mobility decreases with Fe codoping. We note here that the conductivity of these NCs increases with increasing temperature (data not shown) suggesting nonmetallic behavior, unlike bulk Sn-doped  $\text{In}_2\text{O}_3$ .<sup>31</sup> The observed decrease in free electron concentration with Fe doping cannot be explained by a simple substitution of  $\text{In}^{3+}$  with isovalent  $\text{Fe}^{3+}$ . So, why does Fe doping reduce free electron concentration? One possibility could be Fe doping resists Sn to be incorporated in the  $\text{In}_2\text{O}_3$  and therefore lower Sn concentration leading to lower free carrier concentration. However, elemental analysis using ICP-OES and EDAX shows no influence of Fe doping on the concentration of Sn in the codoped sample.<sup>1</sup> Also, no impurity peak was observed in XRD data of Fe–Sn codoped  $\text{In}_2\text{O}_3$  NCs.<sup>1</sup> Another possible reason for reduction of free electron concentration with Fe doping could be that the Sn concentration remains the same producing an equal number of free electrons both in the presence and absence of Fe, but  $\text{Fe}^{3+}$  takes up some of those free electrons converting to  $\text{Fe}^{2+}$ . In fact, prior studies on Fe-doped  $\text{In}_2\text{O}_3$  bulk samples have indicated when the sample is treated under reducing conditions,  $\text{Fe}^{3+}$  can get reduced by consuming the electron obtained from oxygen vacancies as suggested by eq 1.<sup>32</sup> For our NCs, both Fe-doped  $\text{In}_2\text{O}_3$  and Fe–Sn codoped  $\text{In}_2\text{O}_3$ , reaction conditions (oxygen partial pressure) remain the same. However, Sn doping can provide more free electrons following eq 2 to facilitate the reduction of  $\text{Fe}^{3+}$ .

**X-ray Absorption Fine Structure Spectroscopy (XAFS) Explains Why Fe Manipulates Free Electron Concentration in Fe–Sn Codoped  $\text{In}_2\text{O}_3$  NCs.** We employed synchrotron based XAFS for Sn, Fe and In K edge to obtain information around Fe, In, and Sn separately, and then by combining information from each edges, we elucidated the overall local structure of the NC. Figure S4 in the SI compares normalized absorption coefficient at the near edge (XANES) region of the Fe K edge of 5% and 10% Fe doped  $\text{In}_2\text{O}_3$  NCs with those of reference samples: bulk  $\text{FeO}$  and bulk  $\alpha\text{-Fe}_2\text{O}_3$ . In XANES, there are several features that originated from the electronic transition from the core level (1s) to empty electronic levels near the Fermi level, which is largely influenced by their local coordination geometries and oxidation states of Fe ions. Pre-edge peak at 7113 eV (1s → 3d), shoulder (1s → 4s), and crest of the edge (1s → 4p) are marked in Figure 4 showing the representative Fe K edge of Fe-doped and Fe–Sn codoped  $\text{In}_2\text{O}_3$  NCs.<sup>33–36</sup> Both the 5% and 10% Fe doped NC samples exhibit edge crest positions similar to  $\alpha\text{-Fe}_2\text{O}_3$ , suggesting the oxidation state of Fe is 3+ in Fe-doped  $\text{In}_2\text{O}_3$  NCs. However, the spectral features of Fe doped NCs are different from that of  $\alpha\text{-Fe}_2\text{O}_3$  suggesting a different

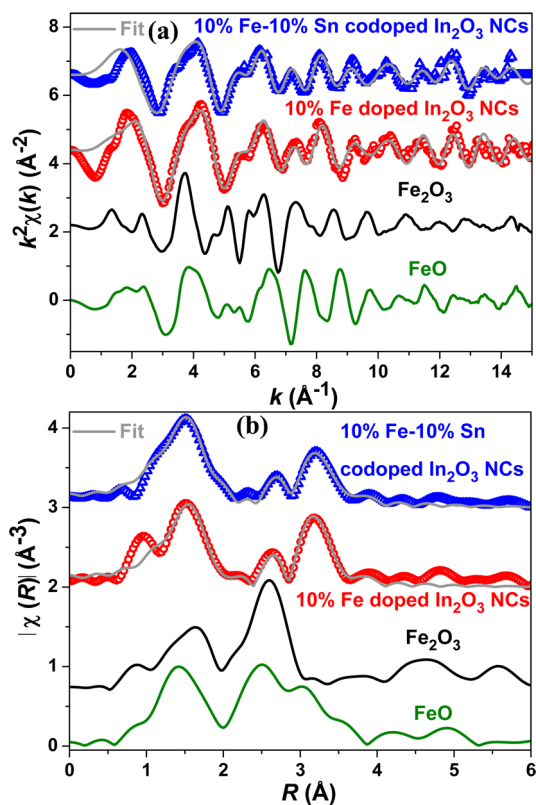


**Figure 5.** Fe K edge EXAFS data for different Fe–Sn codoped  $\text{In}_2\text{O}_3$  NCs. Comparison of (a)  $k^2$  weighted  $\chi(k)$  data and (b) magnitude of Fourier transformed data in R-space of different Fe–Sn codoped NCs with reference samples of bulk  $\text{Fe}_2\text{O}_3$  and  $\text{FeO}$ . Data were shifted vertically for a better representation.

**Table 1.** Fe K Edge EXAFS Fit Results<sup>a</sup>

		10% Fe	10% Fe 10% Sn
Fe–O	N	6.1(9)	5.0(8)
	R (Å)	2.04(1)	2.05(1)
	$\sigma^2$ (Å <sup>2</sup> )	0.010(3)	0.008(3)
Fe–In(Sn)	N	3(1)	4(1)
	R (Å)	3.30(1)	3.31(1)
	$\sigma^2$ (Å <sup>2</sup> )	0.005(2)	0.002(3)
Fe–In(Sn)	N	3(2)	2(1)
	R (Å)	3.76(2)	3.77(2)
	$\sigma^2$ (Å <sup>2</sup> )	0.007(4)	0.003(6)

<sup>a</sup>The fit was performed in R space,  $\chi(R)$  where  $k^2\chi(k)$  was Fourier transformed for  $k = [2, 13 \text{ Å}^{-1}]$ . The fit range  $R = [1, 4 \text{ Å}]$  includes the first neighbor Fe–O and Fe–In/Sn. Including the Fe–Fe bond does not improve the fit quality indicating the Fe–Fe correlation is small. N = coordination number, R = bond length,  $\sigma^2$  = mean square displacement of the distance between the atoms. The photoelectron threshold ( $\Delta E$ ) is used as a variable for the fit. The error bar is written in brackets in the last digit of the fit results.

essentially unaltered for all NC samples. Near edge data (not shown) establish that In is in 3+ oxidation state for all NC samples, as expected. The obtained In–O bond length is 2.17 Å, and two different In–In (or In–Fe or In–Sn) distances are 3.37 and 3.85 Å (Table S2 in the SI). The similarity in the hsecond nearest neighbor data for both Fe-edge and In-edge confirms that that Fe is doped in the  $\text{In}_2\text{O}_3$  NC lattice. For Fe-doped and Fe–Sn doped  $\text{In}_2\text{O}_3$  NCs, the obtained nearest neighbor Fe–O bond length (2.05 Å) is similar to that in  $\text{Fe}_2\text{O}_3$  ( $R = 1.98$  and  $2.08 \text{ Å}$ ) but significantly shorter than In–O bond lengths (2.17 Å). This is expected from the larger ionic radius of  $\text{In}^{3+}$  compared to  $\text{Fe}^{3+}$ , and such differences fade out as we move to second and farther neighbors.<sup>17</sup>

Sn K-edge XANES and EXAFS data of representative samples are shown in Figures S5 and S6 in the SI. Sn near edge data of all NC samples are similar to that of  $\text{SnO}_2$  signifying the oxidation state of Sn is 4+ in all NC samples. The Sn–O bond lengths are 2.05, 2.09, and 2.07 Å for  $\text{SnO}_2$ , 10% Sn doped  $\text{In}_2\text{O}_3$  NCs, and 10% Sn–10% Fe codoped  $\text{In}_2\text{O}_3$  NCs, along with a similar coordination number of 6 (Table S3 of the SI). These observations are consistent with prior studies on Sn doped  $\text{In}_2\text{O}_3$ .<sup>38</sup>  $k^2\chi(k)$  spectra (Figure S7a of the SI) for  $\text{SnO}_2$  and doped NCs are different above  $k = 10 \text{ Å}^{-1}$ . This indicates that the correlations from the second nearest neighbor (in the present case Sn or In) of doped NCs is different from that of  $\text{SnO}_2$  excluding the possibility of segregation of separate  $\text{SnO}_2$ .

These XAFS results (Figure 4 and 5 and Figures S5–S7 in the SI), along with optical properties, XRD patterns, and TEM data suggest the lattice substitution of  $\text{In}^{3+}$  ions with both  $\text{Fe}^{3+}$  and  $\text{Sn}^{4+}$  ions, without forming any detectable impurity phase segregation. Interestingly, in Sn–Fe codoped NCs, a smaller fraction of the  $\text{Fe}^{3+}$  ion gets reduced to  $\text{Fe}^{2+}$  ( $\text{Fe}^{3-\delta}$ ), whereas neither  $\text{In}^{3+}$  nor  $\text{Sn}^{4+}$  changes its oxidation state. Therefore, the only possible way that a fraction of  $\text{Fe}^{3+}$  ions gets reduced is via consuming free electrons obtained from eq 2 via oxidation of interstitial  $\text{O}^{2-}$  to  $\text{O}_2$  gas. Therefore, the free electron concentration reduces in Fe–Sn codoped NCs compared to only Sn-doped NCs, which causes red-shift in the LSPR band (Figure 2) and decreases the electrical conductivity (Figure 3) after incorporating Fe.

**Charge Controlled Magnetic Coupling.** We will now investigate the role of free electrons (arising from Sn) in

including Fe–O, and Fe–In/Sn correlations. For all the NC samples and reference samples, the first nearest neighbor is Fe–O; however, the difference mainly lies in the second and farther nearest neighbor seen at  $R > 2 \text{ Å}$  shown in Figure 5b. Note that the peak of the Fourier amplitude appears at a shorter distance than the actual bond lengths due to the backscattering phase shift of photoelectrons. For, all iron oxide compounds, the second nearest neighbor is Fe–Fe, but for doped NCs, the second nearest neighbor can be Fe–Fe, Fe–In, and Fe–Sn (for Fe–Sn codoped  $\text{In}_2\text{O}_3$  NCs). However, the Fe–Sn correlation cannot be distinguished from Fe–In correlations, since Sn is located immediately after In in the periodic table and, therefore, exhibits very similar backscattering functions.

The best fit parameters (Table 1) show the first neighbor around Fe is oxygen for the doped NCs and fit with 5 to 6 coordination numbers with the Fe–O bond lengths of 2.04 to 2.05 Å for 10% Fe and 10% Fe–10% Sn codoped NCs, respectively. The first Fe–O bond of doped NCs shows higher intensity than  $\text{Fe}_2\text{O}_3$  standards, indicating the bond length distribution (Debye–Waller factor) is smaller for our doped NCs suggesting a more symmetric  $\text{FeO}_6$  octahedron, consistent with the weaker pre-edge for doped NCs in the XANES results (inset to Figure 4). The second neighbor of doped NCs can be fitted with two different Fe–In distances at 3.32 and 3.79 Å. Coordination numbers are somewhat smaller than expected for NC and are often observed in NCs because of the large surface to volume ratio.<sup>15</sup>

Figure S7 in the SI shows EXAFS data for In K edge for representative samples. The In K edge EXAFS remains



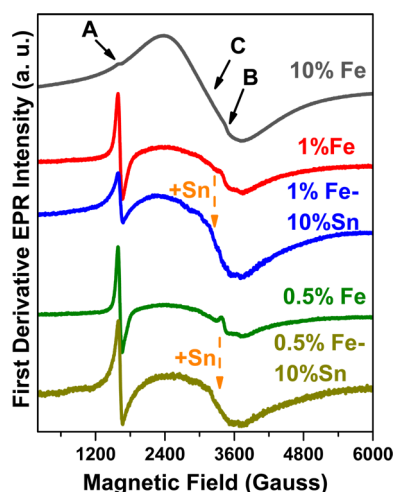


**Figure 6.** EPR spectra measured at 300 K for Fe–Sn codoped  $\text{In}_2\text{O}_3$  NCs with different dopant concentrations.

Fe–Sn codoped  $\text{In}_2\text{O}_3$  NCs. The spectra for 10% Fe-doped  $\text{In}_2\text{O}_3$  NCs is similar to spectra observed in previous literature.<sup>12</sup> The derivative spectrum is governed by a broad signal C (as indicated in Figure 6) with  $g \sim 2.2$  and has been attributed to ferromagnetic resonance (FMR) because of the coupling between electron spins of  $\text{Fe}^{3+}$  ions. Also, there are two other weak derivative EPR signals indicated by arrows A and B, on top of the large background of signal C, as shown in Figure 6. All three EPR signals are because of  $\text{Fe}^{3+}$  ions. Signal A and signal B have been assigned to isolated  $\text{Fe}^{3+}$  with different crystal fields. Signal B with  $g \sim 2.0$  is to  $\text{Fe}^{3+}$  in the octahedral cationic site of the  $\text{In}_2\text{O}_3$  lattice, whereas signal A with  $g \sim 4.3$  corresponds to a lower symmetry rhombic site (possibly distorted octahedral).<sup>12,39</sup>

Our major interest is to study how Sn doping (addition of free electrons) can influence the EPR spectra. Heavily codoped samples such as 10% Sn–10% Fe doped NCs shows EPR spectra (not shown) similar to that of 10% Fe doped NCs, because  $\text{Fe}^{3+}$  ions are located close enough to interact with each other in both samples, even in the absence of free electrons. Therefore, in order to observe any noticeable change due to Sn doping, we chose 0.5% and 1% Fe doping, where the  $\text{Fe}^{3+}$  ions are expected to be at a far distance in such NCs. As expected, Figure 6 shows that the EPR contribution from coupled  $\text{Fe}^{3+}$  ions (broad signal C) decreases significantly with decreasing Fe content from 10% to 1% to 0.5% Fe-doped  $\text{In}_2\text{O}_3$  NCs, thereby, making signals A and B (corresponding to isolate  $\text{Fe}^{3+}$  ions) more prominent. Now, if we compare the EPR spectra after addition of Sn, as shown by the orange arrows in Figure 6, clearly, 1% Fe–10% Sn codoped NCs exhibit more contribution from coupled  $\text{Fe}^{3+}$  ions compared to 1% Fe doped NCs. Particularly, peak B becomes invisible under the background of the broad signal, after Sn doping. Similarly, 0.5% Fe–10% Sn codoped NCs exhibit more contribution from coupled  $\text{Fe}^{3+}$  ions compared to 0.5% Fe doped NCs. This enhancement of coupling between distant  $\text{Fe}^{3+}$  ions just by  $\text{Sn}^{4+}$  doping suggests the free electron mediated magnetic interactions in our Sn and Fe codoped NCs. Figure S8 in the SI shows a small increase in magnetic moment for 1% Fe–10% Sn doped  $\text{In}_2\text{O}_3$  NCs compared to 1% Fe doped  $\text{In}_2\text{O}_3$  NCs.

This enhancement is rather small than the expected increase in magnetic moment via carrier mediated magnetic coupling in the codoped sample. Similarly, we did not observe a significant increase in EPR intensity for the codoped sample. While the broadening of the EPR signal establishes the electron mediated magnetic coupling in codoped NCs, the decrease in magnetic spin via reduction of a fraction of  $\text{Fe}^{3+}$  to  $\text{Fe}^{2+}$  probably opposes the enhancement of EPR intensity that is expected from free electron mediated magnetic coupling. On the other hand,  $\text{Fe}^{2+}$  possesses integral spin exhibiting larger zero-field splitting compared to energy at the X-band and also short spin–lattice relaxation times, making it EPR inactive within our experimental conditions.<sup>40,41</sup> We have also not observed any typical contribution from  $\text{Fe}^{2+}$  ion in the magnetic data of codoped samples. Similar results were also observed in prior reports of semiconductor nanocrystals doped with both  $\text{Fe}^{3+}$  and  $\text{Fe}^{2+}$ ,<sup>40,42</sup> probably because of both the smaller amount of  $\text{Fe}^{2+}$  and the smaller magnetic spin per  $\text{Fe}^{2+}$  compared to  $\text{Fe}^{3+}$  ions.

There are different mechanisms of magnetic coupling in the literature for different dilute magnetic semiconductors.<sup>43,44</sup> Radovanovic et al.<sup>45</sup> recently demonstrated the charge transfer mechanism in Mn doped  $\text{In}_2\text{O}_3$  nanocrystals; however, our Fe–Sn codoped  $\text{In}_2\text{O}_3$  NCs do not exhibit signatures of charge-transfer ferromagnetism. The difference in magnetic interaction may simply stem from the different nature of the samples. Coey et al.<sup>43</sup> suggested magnetic interaction between dopant ions via localized electrons arising from defects. Our NCs exhibiting a strong LSPR band and high electrical conductivity suggest the presence of delocalized free electrons in high concentration. Therefore, free electron mediated magnetic coupling between distant  $\text{Fe}^{3+}$  ion is a more probable mechanism in Sn–Fe codoped NCs.

A similar charge mediated magnetism was previously observed in a magnetically doped semiconductor, for example, in  $\text{Mn}^{2+}$  doped ZnO NCs, but it was a transient excited state phenomenon, where a photogenerated charge carrier was trapped in the excited state under completely inert conditions.<sup>6</sup> There are other reports, where codoping or charge carrier has been found to influence magnetism;<sup>40,46–48</sup> however, electrical conductivity was poor. A higher electrical conductivity of our Fe–Sn codoped NCs along with charge-controlled magnetism is suitable for exhibiting electrical control over magnetism. Apart from dilute magnetic semiconductor type doped NCs, heterostructured NCs such as FePt/PbS magnetic-core/semiconductor-shell also exhibit interesting magneto-electric properties.<sup>49</sup> To the best of our knowledge, our Fe–Sn codoped  $\text{In}_2\text{O}_3$  NC is the only stable system that can exhibit strong LSPR band, good electrical conductivity, and charge controlled magnetism, along with optical transparency in the visible region.

## CONCLUSIONS

We establish the interactions between Fe and Sn dopants, which essentially controls the major properties exhibited by the colloidal Fe–Sn codoped  $\text{In}_2\text{O}_3$  NCs with 6.5 nm average diameter. Lowering of oxygen partial pressure favors the generation of free electrons by shifting equilibrium of eq 2 toward the right-hand side. For example, even with a similar extent of Sn doping, colloidal NCs prepared in air do not show a LSPR band, while NCs prepared under  $\text{N}_2$  or mixture of gases (90%  $\text{N}_2$  and 10%  $\text{H}_2$ ) show a strong LSPR band. In the case of Fe–Sn codoped NCs, a smaller fraction of  $\text{Fe}^{3+}$  ion gets



reduced to  $\text{Fe}^{2+}$  by consuming some free electrons and, therefore, the extent of Fe doping can tune both LSPR band and electrical conductivity. On the other hand,  $\text{Fe}^{3+}$  ions are magnetic dopants with 5 unpaired  $d$ -electrons. Interestingly, free electrons obtained from Sn doping have been found to mediate magnetic coupling among distant  $\text{Fe}^{3+}$  ions via free electron- $\text{Fe}^{3+}$  exchange coupling. Such carrier mediated magnetic coupling is useful for spin based applications. Our present study establishes 10% Fe–10% Sn codoped NCs as a unique multifunctional material that can simultaneously exhibit a LSPR band, high electrical conductivity (2 S/cm), and charge controlled magnetic coupling, in addition to colloidal stability and visible light transparency. Interesting magneto-optic and magneto-electric properties are expected to stem from such interactions between  $\text{Sn}^{4+}$  and  $\text{Fe}^{3+}$  dopants.

## ■ ASSOCIATED CONTENT

### ● Supporting Information

Powder XRD, LSPR absorption, TEM, XANES EXAFS, and magnetic data. This material is available free of charge via the Internet at <http://pubs.acs.org>.

## ■ AUTHOR INFORMATION

### Corresponding Author

\*E-mail: [angshuman@iiserpune.ac.in](mailto:angshuman@iiserpune.ac.in).

### Author Contributions

<sup>‡</sup>These authors contributed equally.

### Notes

The authors declare no competing financial interest.

## ■ ACKNOWLEDGMENTS

We thank Dr. Debraj Choudhury from the University of Arkansas and Dr. Pankaj Mandal and Dr. Pramod Pillai both from IISER Pune for useful discussions. A.N. acknowledges the Science and Engineering Research Board (SERB) for the Ramanujan Fellowship (SR/S2/RJN-61/2012) and the DAE-BRNS grant (2013/20/37C/1/BRNS/954) Govt. of India. We thank the Nanoscience Unit Grant (SR/NM/NS-42/2009) of DST, Govt. of India. G.S.S. acknowledges UGC, Govt. of India, for a junior research fellowship. MRCAT operations are supported by the Department of energy and MRCAT host institutions. Use of the Advanced Photon Source was supported by the U.S. Department of Energy, Office of Science, Office of Basic Energy Sciences, under Contract No. DE-AC02-69-06CH11357.

## ■ REFERENCES

- (1) Tandon, B.; Shanker, G. S.; Nag, A. J. *Phys. Chem. Lett.* **2014**, *5*, 2306–2311.
- (2) Kim, J.; Park, S.; Lee, J. E.; Jin, S. M.; Lee, J. H.; Lee, I. S.; Yang, I.; Kim, J. S.; Kim, S. K.; Cho, M. H.; Hyeon, T. *Angew. Chem., Int. Ed.* **2006**, *45*, 7754–7758.
- (3) Dong, W. J.; Li, Y. S.; Niu, D. C.; Ma, Z.; Gu, J. L.; Chen, Y.; Zhao, W. R.; Liu, X. H.; Liu, C. S.; Shi, J. L. *Adv. Mater.* **2011**, *23*, 5392–5397.
- (4) Hessel, C. M.; Pattani, V. P.; Rasch, M.; Panthani, M. G.; Koo, B.; Tunnell, J. W.; Korgel, B. A. *Nano Lett.* **2011**, *11*, 2560–2566.
- (5) Tian, Q. W.; Hu, J. Q.; Zhu, Y. H.; Zou, R. J.; Chen, Z. G.; Yang, S. P.; Li, R. W.; Su, Q. Q.; Han, Y.; Liu, X. G. *J. Am. Chem. Soc.* **2013**, *135*, 8571–8577.
- (6) Ochsenbein, S. T.; Feng, Y.; Whitaker, K. M.; Badaeva, E.; Liu, W. K.; Li, X. S.; Gamelin, D. R. *Nat. Nanotechnol.* **2009**, *4*, 681–687.
- (7) Gilstrap, R. A.; Capozzi, C. J.; Carson, C. G.; Gerhardt, R. A.; Summers, C. J. *Adv. Mater.* **2008**, *20*, 4163–4166.

- (8) Kanehara, M.; Koike, H.; Yoshinaga, T.; Teranishi, T. *J. Am. Chem. Soc.* **2009**, *131*, 17736–17737.
- (9) Li, S. Q.; Guo, P. J.; Zhang, L. X.; Zhou, W.; Odom, T. W.; Seideman, T.; Ketterson, J. B.; Chang, R. P. H. *ACS Nano* **2011**, *5*, 9161–9170.
- (10) Lee, J.; Lee, S.; Li, G. L.; Petruska, M. A.; Paine, D. C.; Sun, S. H. *J. Am. Chem. Soc.* **2012**, *134*, 13410–13414.
- (11) Lounis, S. D.; Runnerstrom, E. L.; Bergerud, A.; Nordlund, D.; Milliron, D. J. *J. Am. Chem. Soc.* **2014**, *136*, 7110.
- (12) Singhal, A.; Achary, S. N.; Manjanna, J.; Jayakumar, O. D.; Kadam, R. M.; Tyagi, A. K. *J. Phys. Chem. C* **2009**, *113*, 3600–3606.
- (13) Nag, A.; Chakraborty, S.; Sarma, D. D. *J. Am. Chem. Soc.* **2008**, *130*, 10605–10611.
- (14) Nag, A.; Chung, D. S.; Dolzhnikov, D. S.; Dimitrijevic, N. M.; Chattopadhyay, S.; Shibata, T.; Talapin, D. V. *J. Am. Chem. Soc.* **2012**, *134*, 13604–13615.
- (15) Rao, M. J.; Shibata, T.; Chattopadhyay, S.; Nag, A. *J. Phys. Chem. Lett.* **2014**, *5*, 167–173.
- (16) Becker, M. A.; Radich, J. G.; Bunker, B. A.; Kamat, P. V. *J. Phys. Chem. Lett.* **2014**, *5*, 1575–1582.
- (17) Mukherjee, S.; Nag, A.; Kocovski, V.; Santra, P. K.; Balasubramanian, M.; Chattopadhyay, S.; Shibata, T.; Schaefer, F.; Ruzs, J.; Gerard, C.; Eriksson, O.; Segre, C. U.; Sarma, D. D. *Phys. Rev. B* **2014**, *89*, 224105.
- (18) Wang, Y. S.; Thomas, P. J.; O'Brien, P. J. *Phys. Chem. B* **2006**, *110*, 21412.
- (19) Buonsanti, R.; Milliron, D. J. *Chem. Mater.* **2013**, *25*, 1305.
- (20) Dhara, B.; Ballav, N. *RSC Adv.* **2013**, *3*, 4909.
- (21) [www.mrcat.iit.edu](http://www.mrcat.iit.edu) (accessed Dec 21, 2014).
- (22) Stern, E. A.; Heald, S. M. *Rev. Sci. Instrum.* **1979**, *50*, 1579–1582.
- (23) Ravel, B.; Newville, M. J. *Synchrotron Radiat.* **2005**, *12*, 537–541.
- (24) Wang, T.; Radovanovic, P. V. *J. Phys. Chem. C* **2011**, *115*, 406.
- (25) Shim, M.; Guyot-Sionnest, P. *J. Am. Chem. Soc.* **2001**, *123*, 11651–11654.
- (26) Fauchaux, J. A.; Jain, K. J. *Phys. Chem. Lett.* **2013**, *4*, 3024–3030.
- (27) Gonzalez, G. B. *Materials* **2012**, *5*, 818–850.
- (28) Frank, G.; Kostlin, H. *Appl. Phys. A: Mater. Sci. Process.* **1982**, *27*, 197.
- (29) Warschkow, O.; Ellis, D. E.; Gonzalez, G. B.; Mason, T. O. *J. Am. Ceram. Soc.* **2003**, *86*, 1707–1711.
- (30) Luther, J. M.; Jain, P. K.; Ewers, T.; Alivisatos, A. P. *Nat. Mater.* **2011**, *10*, 361.
- (31) Ba, J. H.; Fattakhova-Rohlfing, D.; Feldhoff, A.; Brezesinski, T.; Djerdj, I.; Wark, M.; Niederberger, M. *Chem. Mater.* **2006**, *18*, 2848.
- (32) Yu, Z. G.; He, J.; Xu, S. F.; Xue, Q. Z.; van't Erve, O. M. J.; Jonker, B. T.; Marcus, M. A.; Yoo, Y. K.; Cheng, S. F.; Xiang, X. D. *Phys. Rev. B* **2006**, *74*, 104111.
- (33) Berry, A. J.; O'Neill, H. S. C.; Jayasuriya, K. D.; Cambell, S. J.; Foran, G. J. *Am. Mineral.* **2003**, *88*, 967–977.
- (34) Cottrell, E.; Kelly, K. A.; Lanzirrotti, A.; Fischer, R. A. *Chem. Geol.* **2009**, *268*, 167–179.
- (35) Wilke, M.; Farges, F.; PeTit, P. E.; Brown, G. E., Jr.; Martin, F. *Am. Mineral.* **2001**, *86*, 714–730.
- (36) Westre, T. E.; Kennepohl, P.; DeWitt, J. G.; Hedman, B.; Hodgson, K. O.; Solomon, E. I. *J. Am. Chem. Soc.* **1997**, *119*, 6297–6314.
- (37) Chen, L. X.; Liu, T.; Thurnauer, M. C.; Csencsits, R.; Rajh, T. *J. Phys. Chem. B* **2002**, *106*, 8539–8546.
- (38) Mason, T. O.; Kammler, D. R.; Ingram, B. J.; Gonzalez, G. B.; Young, D. L.; Coutts, T. J. *Thin Solid Films* **2003**, *445*, 186–192.
- (39) Chakradhar, R. P. S.; Yasoda, B.; Rao, J. L.; Gopal, N. O. *Mater. Res. Bull.* **2006**, *41*, 1646.
- (40) Karmakar, D.; Mandal, S. K.; Kadam, R. M.; Paulose, P. L.; Rajarajan, A. K.; Nath, T. K.; Das, A. K.; Dasgupta, I.; Das, G. P. *Phys. Rev. B* **2007**, *75*, 144404.

- 736 (41) Misra, S. K.; Diehl, S.; Tipikin, D.; Freed, J. H. *J. Magn. Reson.*  
737 **2010**, 205, 14.
- 738 (42) Chu, D. W.; Zeng, Y. P.; Jiang, D. L.; Ren, Z. M.; Ren, W. L.;  
739 Wang, J. H.; Zhang, T. *J. Mater. Res.* **2008**, 23, 2597.
- 740 (43) Coey, J. M. D.; Venkatesan, M.; Fitzgerald, C. B. *Nat. Mater.*  
741 **2005**, 4, 173.
- 742 (44) Farvid, S. S.; Hegde, M.; Radovanovic, P. V. *Chem. Mater.* **2013**,  
743 25, 233.
- 744 (45) Farvid, S. S.; Sabergharesou, T.; Huffluss, L. N.; Hegde, M.;  
745 Prouzet, E.; Radovanovic, P. V. *J. Am. Chem. Soc.* **2014**, 136, 7669–  
746 7679.
- 747 (46) Zheng, W. W.; Strouse, G. F. *J. Am. Chem. Soc.* **2011**, 133,  
748 7482–7489.
- 749 (47) May, J. W.; McMorris, R. J.; Li, X. S. *J. Phys. Chem. Lett.* **2012**, 3,  
750 1374–1380.
- 751 (48) Viswanatha, R.; Naveh, D.; Chelikowsky, J. R.; Kronik, L.;  
752 Sarma, D. D. *J. Phys. Chem. Lett.* **2012**, 3, 2009–2014.
- 753 (49) Lee, J. S.; Bodnarchuk, M. I.; Shevchenko, E. V.; Talapin, D. V.  
754 *J. Am. Chem. Soc.* **2010**, 132, 6382–6391.